JPE 19-5-17

https://doi.org/10.6113/JPE.2019.19.5.1235
ISSN(Print): 1598-2092 / ISSN(Online): 2093-4718

Modeling and Design of Zero-Voltage-Switching Controller for Wireless Power Transfer Systems Based on Closed-Loop Dominant Pole

Cheng Chen*, Hong Zhou*, Qijun Deng†,*, Wenshan Hu*, Yanjuan Yu*, Xiaoqing Lu*, and Jingang Lai**

*School of Electrical Engineering and Automation, Wuhan University, Wuhan, China
†Shenzhen Research Institute, Wuhan University, Shenzhen, China
**E.ON Energy Research Center, RWTH Aachen University, Aachen, Germany

Abstract

Zero-Voltage-Switching (ZVS) operation for a Wireless Power Transfer (WPT) system can be achieved by designing a ZVS controller. However, the performance of the controller in some industrial applications needs to be designed tightly. This paper introduces a ZVS controller design method for WPT systems. The parameters of the controller are designed according to the desired performance based on the closed loop dominant pole placement method. To describe the dynamic characteristics of the system ZVS angle, a nonlinear dynamic model is deduced and linearized using the small signal linearization method. By analyzing the zero-pole distribution, a low-order equivalent model that facilitates the controller design is obtained. The parameters of the controller are designed by calculating the time constant of the closed-loop dominant poles. A prototype of a WPT system with the designed controller and a five-stage multistage series variable capacitor (MSVC) is built and tested to verify the performance of the controller. The recorded response curves and waveforms show that the designed controller can maintain the ZVS angle at the reference angle with satisfactory control performance.

Key words: Dominant pole, Modeling, Wireless power transfer, Zero-voltage-switching control

I. INTRODUCTION

Magnetically coupled resonant wireless power transfer (WPT) has been proven to be a superior technology for the charging of a variety of electrical devices, such as electric vehicles (EVs) [1]-[3], biomedical implants [4], [5], [9], portable equipment [6] and so on, without the need for metallic media. A typical WPT system consists of a DC voltage source, inverter, resonant network, rectifier and load. To reduce the switching loss of the inverter, the system needs to realize zero-voltage-switching (ZVS) operation in the full charging period. However, because of fluctuations in battery resistance [1]-[3], the designed input impedance point of the system may dynamically drift away, which leads to unstable ZVS operation and degradation of the transmission efficiency.

Manuscript received Oct. 19, 2018; accepted May 29, 2019
Recommended for publication by Associate Editor Fuxin Liu.
†Corresponding Author: dqj@whu.edu.cn
Tel: +86-18971636308, Wuhan University
*School of Electrical Engineering and Automation, Wuhan Univ., China
**E.ON Energy Research Center, RWTH Aachen University, Germany

To solve this significant challenge, numerous control methods have been proposed. In these studies, the operating frequency and impedance matching circuit are usually used as the controlled objects of the controller, that is frequency control (FC) and impedance matching control (IMC). Meanwhile, the phase difference between the primary current and the output voltage of the inverter is detected to form a feedback control loop. Typically, the drive signal of the inverter can be tuned by a proportional integral (PI) controller [3], amplifier controller [4] or phase locked loop (PLL) [5], [7] to achieve ZVS operation. However, the design process of the frequency controllers is not fully discussed in these research projects. In an effort to improve transmission efficiency, zero-phase-difference capacitance control (ZPDCC) [8], PLL [9], [10] and algorithm control [11]-[15] were proposed to regulate the phase angle of the input impedance of an inverter using variable capacitors. Although the efficiency and ZVS operation of the system can be improved and realized, respectively, the control performance of the controller is not optimized. In [16], [17], frequency controllers through PI action are proposed to

© 2019 KIPE

track the ZVS operation curve. To optimize control performance, an empirical Ziegler–Nichols (ZN) method is adopted. However, the dynamic characteristics of the system are neither analyzed nor considered in the controller design process, which results in inaccurate parameters for the controller. Also, considering that the dynamics of the second-order generalized integrator phase-locked loop (SOGI-PLL) can be easily analyzed, a direct phase control (DPC) approach [18] is developed to provide ZVS operation for WPT systems. Compared with [5], [7], [9], [10], a good transient response and a low overshoot can be achieved for the SOGI-PLL. However, the dynamics of the full system are still not analyzed.

It is well known that an analytical model of a full system and its dynamic characteristics are necessary for designing a controller. Furthermore, in many industrial applications regardless of whether it is a frequency or an impedance matching control method, the control performances of the system, such as the settling time and overshoot, need to be designed tightly in terms of the system requirements. Therefore, an appropriate dynamic model of the full system is required to analyze the input-output characteristics and to design accurate parameters for the controllers.

In the past decades, WPT systems have been modeled using the frequency domain modeling method [3], [18], Laplace phasor transform method [17] or generalized state space averaging (GSSA) technique [18]-[26]. However, some obstacles to these methods make it difficult to directly design a ZVS controller. The frequency domain modeling method cannot dynamically describe the electrical behavior of systems, and the internal state variables of the Laplace phasor transform method are unobservable, which makes the model unable to describe the full dynamics of a system. In addition, the GSSA technique increases the model's order because it uses two slowly varying state variables to describe a fast varying state variable. Most importantly, these models have difficulty directly describing the dynamic characteristic of ZVS operation. For example, the authors of [27] proposed two transfer function models for the control-to-output corresponding to the charging modes. Although the phase and gain margin of the control loops can be analyzed and optimized through the proposed transfer functions, an additional current stress optimization controller is required on the primary side to maintain the ZVS operation. Thus, the relationship between the circuit state variables and the phase angle needs to be derived to describe the ZVS operation. Fortunately, based on the coupled-mode theory [28], a dynamic model covering the phase angles and amplitudes of the coupling network is obtained in [29], [30]. Because the state variables of the dynamic differential equation can be replaced by the phase angle and the amplitude of the coupled modes, a dynamic analysis for the full system and ZVS operation can be directly obtained.

The main purpose of this paper is to provide a ZVS controller design method for WPT systems. The parameters of the controller are designed according to the desired performance based on the closed loop dominant pole placement method. Thus, to describe the dynamic characteristics of the system ZVS angle, a nonlinear dynamic model is deduced and linearized, where the operating frequency or the controllable impedance matching network is the input, and the ZVS angle is the output. Meanwhile, by analyzing the zero-pole distribution of the linearized model, a low-order equivalent transfer function model that facilitates the PI controller design is achieved. The parameters of the controller are designed by calculating the time constant of the closed-loop dominant poles. To validate the proposed controller design method and control performance, a five-stage MSVC is set up as an actuator in the experiment. By comparing it with existing literature [3]-[18], the advantages of the proposed controller design method in this paper are as follows.

(1) The dynamic characteristics of the system ZVS angle can be described in the proposed model. In addition, both the frequency and impedance matching controllers can be designed.

(2) Based on the zero-pole distribution of the dynamic model, the stability of the control loop and the characteristics of the zero-pole can be analyzed. In order to facilitate the controller design, a low-order equivalent transfer function model that consists of dominant poles is obtained.

(3) When compared with the empirical equation based method in [16], [17], the parameters of the ZVS controller are designed by calculating the time constant of the closed-loop dominant poles according to the desired performance. Therefore, the controller is especially useful when a WPT system needs to be designed tightly in terms of its preset settling time and overshoot.

This paper is organized as follows: Section II analyzes the main circuit of the proposed system and proposes a ZVS control strategy. Section III focuses on the modeling of the equivalent circuit and the MSVC. Section IV quantitatively analyzes the dynamic characteristics of the linear model and designs three PI controllers according to different requirements. A prototype circuit is set up in section V to verify the proposed controller design method and its control performance. Some conclusions are given in section VI.

II. Analysis of the System Structure and the ZVS Control Strategy

A. Power Stage

A series–series compensated topology of the WPT system is shown in Fig. 1, which consists of a DC input voltage V_{I}, a full-bridge inverter, two resonant tanks, a rectifier and a battery load R_{b}. Each resonant tank comprises a series capacitor C_{n}, inductor L_{n} and its equivalent series resistor (ESR) R_n (n=1, 2), respectively. C_{f} and M are the filter capacitor and the mutual inductance between the two coils. During the

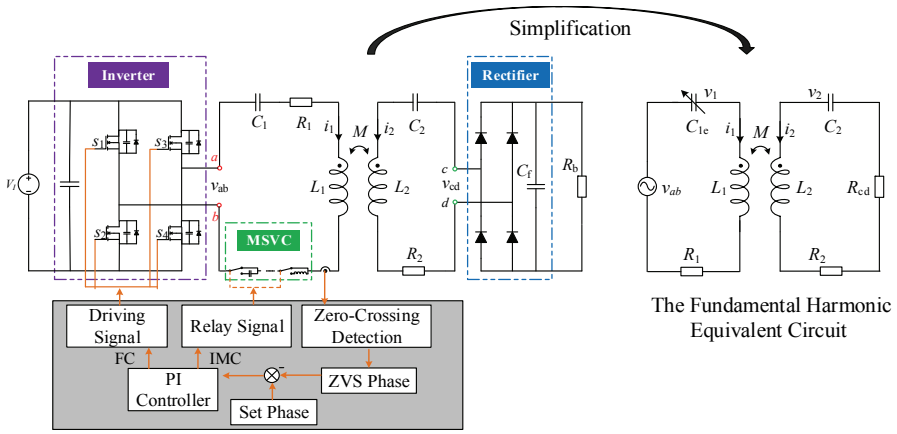

Fig. 1. Topology circuit of the analyzed wireless charging system.

charging process, the full-bridge inverter converts the DC voltage into a quasi-square wave to energize the resonant network. Then, the full-bridge rectifier converts the AC current into a DC current to wirelessly charge the battery.

In order to achieve ZVS control, the operating frequency and the MSVC in the primary side are usually used as the controlled objects to form FC or IMC closed-loops. In detail, by detecting the zero-crossing of the primary resonance current i_1 and the rising edge of the inverter gate-driving signal, the phase difference between i_1 and v_{ab} can be obtained to predict the status of the ZVS operation. Then, the PI controller converts the angle errors into control signals for the MOSFETs or relays to adjust the operating frequency or equivalent capacitance of the MSVC, respectively.

B. Circuit Equivalent and ZVS Control Strategy

The equivalent of any circuit is necessary for developing a model and for designing a controller. In this section, the equivalent circuit for a WPT system is derived based on the following assumptions.

(1) The resonant currents i_1 and i_2 through the compensation network are sinusoidal, and the operation frequency is ω_s.

(2) All of the resonant capacitors and inductors are identical.

(3) The filter capacitance of the full-bridge rectifier is large enough.

Therefore, the fundamental components of the output voltage of the inverter and the equivalent resistance of the rectifier load can be respectively written as:

$$v_{ab} = V_1 \operatorname{sgn}\left(\omega_s t\right), \tag{1}$$

$$R_{cd} = \frac{8}{\pi^2} R_b . \tag{2}$$

Considering (1) and (2), the main circuit of a WPT system can be simplified to an equivalent coupled circuit as shown in Fig. 1. The notation C_{1e} in the equivalent coupled circuit represents the equivalent capacitance of the capacitor C_1 in series with the multistage series variable capacitor (MSVC).

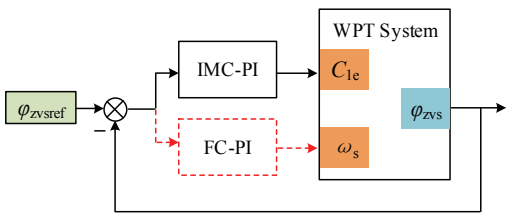

Fig. 2. Control diagram of the IMC and FC methods for ZVS operation.

The input impedance Z_{in} of the equivalent circuit can be expressed as follows:

$$Z_{in} = Z_1 + \frac{\left(\omega_s M\right)^2}{\left(Z_2 + R_{cd}\right)} = R_1 + j\omega_s L_1 + \frac{1}{j\omega_s C_{1e}} + \frac{\left(\omega_s M\right)^2}{Z_2 + R_{cd}}, \tag{3}$$

where Z_1 and Z_2 stand for the primary and secondary resonant network impedances, respectively. Therefore, the ZVS angle φ_{zvs} can be depicted as [3]:

$$\begin{aligned} \varphi_{zvs} &= \Delta\varphi - \varphi_d \\ &= \arctan\left(\frac{\operatorname{Im}\left[Z_{in}\right]}{\operatorname{Re}\left[Z_{in}\right]}\right) - \frac{\left(1 - D_{inv}\right)\pi}{2} . \end{aligned} \tag{4}$$

The symbol $\Delta\varphi$ is the input impedance angle of Z_{in}, and φ_d is the dead-time phase angle. D_{inv} refers to the duty cycle of the square wave drive signal for the MOSFETs. By analyzing (3) and (4), it is possible to draw a conclusion that the ZVS angle φ_{zvs} can remain a constant by regulating the capacitance of C_{1e}, or the angular switching frequency ω_s of the inverter. In other words, the ZVS operation can be obtained by both FC and IMC methods. Therefore, a control diagram of the FC and IMC methods for ZVS operation is proposed in Fig. 2, and the operation principle of this strategy is briefly explained as follows.

First, the zero crossing of the primary current is detected by the measuring circuit and processor. Then, the ZVS angle can be calculated by (4). By comparing this value with the reference angle, the angle errors are converted into new control quantities for the corresponding control object by the

PI controller. Taking the IMC method as an example, the ZVS angle φ_{zvs} follows the reference angle after several adjustments on the MSVC to achieve ZVS operation.

III. Dynamic Modeling of the Proposed WPT System

A. Dynamic Model of a Coupled Network

According to the fundamental harmonic equivalent circuit of the system shown in Fig. 1, the electrical behavior of the coupled network can be described by the following fourth order dynamic differential equations:

$$\begin{cases} v_{ab} = v_1 + i_1 R_1 + L_1 \dfrac{di_1(t)}{dt} + M \dfrac{di_2(t)}{dt} \\ i_1 = C_{1e} \dfrac{dv_1(t)}{dt} \\ M \dfrac{di_1(t)}{dt} = v_2 - i_2 (R_2 + R_{cd}) - L_2 \dfrac{di_2(t)}{dt} \\ i_2 = C_2 \dfrac{dv_2(t)}{dt} \end{cases}, \tag{5}$$

where i_1 and i_2 are the resonance currents through the primary and secondary coils, and v_1 and v_2 are the voltages across the primary and secondary resonance capacitors. Similar to the equivalent circuit models in [19]-[25], these equations cannot directly analyze the ZVS characteristics. Therefore, it is necessary to establish the relationship between the state variables in (5) and the phase angle of the coupled network.

According to [29], [30], the dynamic characteristics of a coupled network can also be described by the coupled-mode theory [28]. Based on this suggestion, it can be assumed that the amplitude and phase angle of the primary coupled mode are a_1 and θ_1, respectively. Similar definitions of a_2 and θ_2 are for the secondary side. As a result, the state variables in (5) can be represented by a_n and θ_n as [29], [30] follows:

$$\begin{cases} i_n = \sqrt{\dfrac{2}{L_n}} \cdot a_n \cos(\omega_s t + \theta_n) \\ v_n = \sqrt{\dfrac{2}{C_n}} \cdot a_n \sin(\omega_s t + \theta_n) \end{cases}. \tag{6}$$

By substituting (6) into (5) and averaging the model in a switching period [29], one obtains a nonlinear time-invariant averaged model for the equivalent circuit as follows:

$$\dot{x} = f(x) + g(x)u, \tag{7}$$

where x= [a_1, θ_1, a_2, θ_2] T is the state vector, and u=[C_{1e}, ω_s] is the input of the model. f(x) and g(x) are smooth nonlinear functions, namely:

$$f(x) = \begin{pmatrix} K_1(-L_2K_3 - MK_4K_8 + MK_5K_9 + L_2K_6\cos x_2) \\ -\dfrac{K_1}{x_1}(MK_4K_9 + MK_5K_8 + L_2K_6\sin x_2) \\ K_2(-L_1K_5 + MK_3K_9 - MK_6\cos x_4) \\ -\dfrac{K_2}{x_3}(-L_1K_4 - MK_3K_8 - MK_6\sin x_4) \end{pmatrix}, \tag{8}$$

$$g(x) = \frac{1}{2\Delta}\begin{Bmatrix} 0 & 0 \\ (2L_1L_2 - M^2)K_7 / \sqrt{L_1} & -1 \\ -M\sqrt{L_2}x_1K_7K_8 & 0 \\ M\sqrt{L_2}x_1K_7K_9 / x_3 & -1 \end{Bmatrix}. \tag{9}$$

The variables K_1-K_9 are listed in the Appendix. According to (4), the output of (7) can be depicted as:

$$h_{ZVS}(x) = -\frac{180}{\pi}\left(x_2 + \frac{(1 - D_{inv})\pi}{2}\right). \tag{10}$$

By linearization around the operating point, it is possible to obtain a linearized small signal model for the WPT system.

B. Model Linearization

The model as per (7) through (10) represents the envelope of the ZVS angle under both steady-state and transient conditions. In other words, it contains both the operating point and the small-signal model. Thus, each variable in this model can be written as the sum of the operation point, and the small perturbation around it as:

$$x = x_o + \Delta x, \tag{11}$$

where x_o is the steady operation point of the state variables in (7), and Δx is the transient small-signal condition. By substituting (11) into (7)-(10), the nonlinear time-invariant averaged model can be linearized around the operating point x_o using Taylor's series expansion, and written in the state-space form as:

$$\begin{cases} \Delta\dot{x} = \mathbf{A}\cdot\Delta x + \mathbf{B}\cdot\Delta u \\ \Delta y = \mathbf{C}\cdot\Delta x \end{cases}, \tag{12}$$

where **A**, **B** and **C** are the partial derivative matrices.

It can be seen from (12) that this linear model includes both the frequency control (FC) and the impedance matching control (IMC) methods. In the FC method, the parameters of the resonant circuit can generally be regarded as constants, and the operating frequency is selected as the input of the model. Conversely, the operating angular frequency ω_s in the IMC method can be removed, and the impedance matching network is developed as the actuator in the control loop.

Since the dynamic analysis and controller design for both the FC and IMC methods are similar, only the IMC method is considered as an example in the following sections. Thus, the operating angular frequency ω_s in the input matrix and the second column of matrix **B** will be removed hereafter.

A simple multistage series variable capacitor (MSVC) regulated by a controlling quantity d is selected in this paper by combined consideration of the regulation range, precision and costs. This is because the implementation process of the MSVC is convenient and the relationship between the control quantity and the equivalent capacitance is not complicated.

C. Development of Multistage Series Variable Capacitor

In order to obtain the relationship between the control

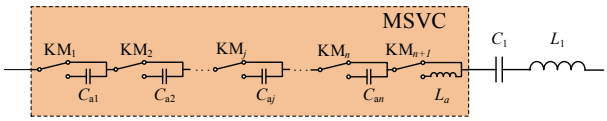

Fig. 3. Topology circuit of a multistage series variable capacitor.

quantity and the equivalent capacitance, the proposed MSVC needs to be modeled. Fig. 3 shows the configuration of the proposed MSVC. It consists of multiple capacitors C_{an} (n=1, 2, …) and an inductor L_a, where n is the number of capacitors and j represents the j^{th} capacitor in the MSVC. The capacitance C_{aj} (j=1,2,…,n) is designed as per:

$$C_{aj} = \frac{C_a}{2^{j-1}}, \tag{13}$$

to construct a geometric capacitance array $\{C_{a1}, C_{a2}, \ldots C_{an}\}$. The first term C_{a1}=C_a is the maximum capacitance, and the inductance L_a is defined as:

$$L_a = \frac{1}{\omega_s^2}\sum_{j=1}^{n}\frac{1}{C_{aj}}. \tag{14}$$

Each capacitor and inductor in the MSVC is controlled by a single-pole-double-throw (SPDT) relay, respectively, which can be connected to the resonant circuit or not. The SPDT relays are driven by an n+1 bit binary array $\{p_1, p_2, \ldots, p_j, \ldots, p_n, p_{n+1}\}$, where p_n can be 0 or 1 corresponding to the relay statuses of ON or OFF. The notation p_j represents the relay of the j^{th} capacitor. Therefore, the operational status of the MSVC can be expressed by a signed decimal control quantity.

$$d = (-1)^{p_{n+1}+1}\times\left(p_n\times 2^{j-1} + p_{n-1}\times 2^{j-2} + \cdots + p_1\times 2^0\right). \tag{15}$$

As a result, the equivalent capacitance of the capacitor C_1 in series with the MSVC is:

$$C_{1e} = \begin{cases} \dfrac{L_1+L_a}{L_1}\dfrac{C_1C_a}{C_a+\left(2^{n-2}-d\right)C_1} & d \ge 0 \\ \dfrac{C_1C_a}{C_a - dC_1} & d < 0 \end{cases}. \tag{16}$$

It can be seen that from (16), the equivalent capacitance C_{1e} has a bidirectional adjustment range, and its adjustment range and accuracy are related to the number n and the maximum capacitance C_a of the capacitors. Furthermore, according to the combination of (3)-(4) and (16), the ZVS angle φ_{zvs} can be regulated by the control quantity d. By substituting (16) into (7), a model with d as the input and a ZVS angle as the output can be achieved. Namely, a constant ZVS angle can be realized by designing a controller to automatically adjust the MSVC.

IV. Model Analysis and Controller Parameter Design

A.Model Dynamic Characteristics Analysis and Reduction

To linearize the nonlinear model, the steady-state operating point should be calculated by setting the derivative terms in (7) to zero. According to the full-bridge inverter minimum ZVS phase angle studied in [31], the preset ZVS angle can be calculated by:

$$\Delta\varphi_{\min} \ge \arccos\left(1 - \frac{2\omega_s C_{oss} V_1}{I_1}\right), \tag{17}$$

where C_{oss}=400 pF is the capacitance of the capacitor paralleled with the transistor, and I_1 is the magnitude of the current flowing through the MOSFET. Therefore, the preset ZVS angle is selected to be 5° in this paper. According to the key parameters of the system in Table I, it is possible to obtain the operating point of the system by:

$$x_0 = \begin{bmatrix}0.01 & -0.09 & 0.01 & -1.51\end{bmatrix}^{\text{T}}. \tag{18}$$

The substitution of x_o and the circuit parameters into (12) yields the partial derivative matrices of the IMC linear model as:

$$\mathbf{A} = \begin{bmatrix} -2258.4 & -19 & -21383 & 44 \\ 2.1e5 & -2258.6 & -3.8e5 & -26730 \\ 21437 & 31 & -17116 & -37.4 \\ -2.7e5 & 17149 & 2.6e5 & -17116 \end{bmatrix}, \tag{19}$$

$$\mathbf{B} = \begin{bmatrix}0 & -486.4 & -0.05 & 0.67\end{bmatrix}^{\text{T}}, \tag{20}$$

$$\mathbf{C} = \begin{bmatrix}0 & -57.3 & 0 & 0\end{bmatrix}. \tag{21}$$

Using MATLAB, a fourth-order linear small signal open-loop transfer function model for the equivalent circuit can be expressed as per:

$$G(s) = \frac{2.79e^4\left(s+1.68e4\right)\left(s^2+1.97e4s+5.2e8\right)}{\left(s^2+2.04e4s+5.1e8\right)\left(s^2+4.6e4s+9.67e8\right)}, \tag{22}$$

TABLE I
Key Parameters of the System

Parameters	Values
Inductance on primary side L_1	261.38 μH
Capacitance on primary side C_1	1043 pF
ESR of primary side R_1	1.11 Ω
Inductance on secondary side L_2	264.1 μH
Capacitance on secondary side C_2	1050.1 pF
ESR of secondary side R_2	0.92 Ω
Mutual inductance between two coils M	6 μH
Input DC voltage V_1	10 V
Switching frequency of the inverter f_s	301.8 kHz
Load resistance R_b	10 Ω
Control quantity of the MSVC d_o	25
Duty cycle of drive signal for inverter D_{inv}	45 %
Rising time of the MOSFET t_r	28 ns
Falling time of the MOSFET t_f	8 ns
On resistance of the MOSFET r_{MOS}	40 mΩ
MOSFET's drain-source capacitance C_{ds}	320 pF
ESR of filter capacitor r_{Cf}	5 mΩ
On resistance of the rectifier diodes r_D	5 mΩ
Forward voltage of rectifier diodes V_D	0.7 V

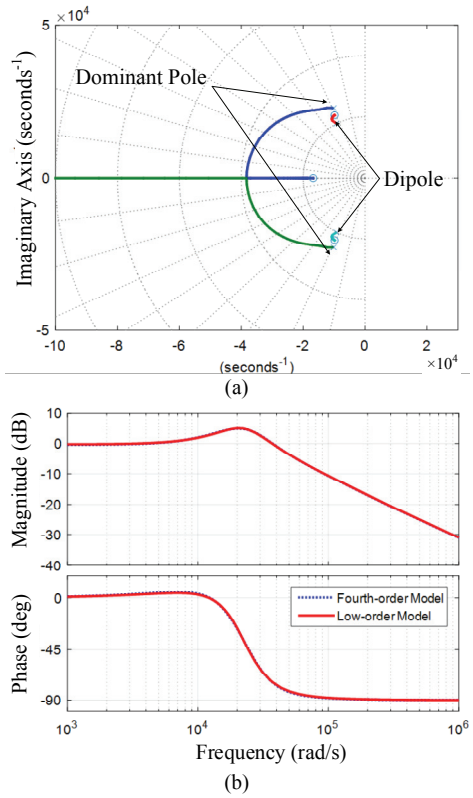

Fig. 4. Root locus and bode plot of a unity feedback system. (a) Root locus of the fourth-order linear small signal model. (b) Bode plot of the low-order model and fourth-order linear small signal model.

with the control quantity d of the MSVC as the input, and the ZVS angle φ_{zvs} as the output. The unity feedback root locus of this transfer function model is plotted in Fig. 4(a). By analyzing the closed-loop zero-pole distribution, the following conclusion can be obtained.

(1) The stability of the unity feedback system is available because the closed-loop poles, which are composed of two plural dipole pairs and two plural dominant poles, are all located in the left *s*-plane.

(2) According to the zero-pole distribution, the dipoles in Fig. 4(a) have less influence on the dynamic characteristics of the system since the distance between the zero and pole of the dipole is much smaller than its module from the origin. Hence, after several adjustments of the gain and coefficient of the dominant pole, (22) can be equivalent to a low-order model.

According to the results of the analysis, a low-order open-loop transfer function model for the equivalent circuit can be obtained as:

$$G(s)=\frac{2.8e4s+5e8}{s^2+2.06e4+5.1e8}. \tag{23}$$

A Bode plot of this low-order model and the original fourth-order linearized small signal model are plotted in Fig. 4(b). This figure shows that the low-order model has the same magnitude-frequency and phase-frequency characteristics as the original model, which proves that the low-order model is accurate.

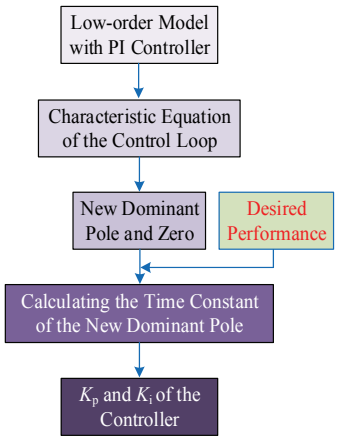

Fig. 5. Flow chart of the proposed PI controller parameter design method.

B. Design of the PI Controller Parameter

The transfer function of the PI controller is:

$$G_c(s)=K_p+\frac{K_i}{s}, \tag{24}$$

where K_p and K_i are the proportional and integral parameters. A flow chart of the proposed PI controller parameter design method is shown in Fig. 5. It can be seen that the control loop consists of a low-order model and a PI controller. After the closed loop characteristic equation of the control loop is obtained, the parameters of the PI controller can be achieved by calculating the time constant of the new dominant pole in terms of a desired performance.

According to the control strategy in Fig. 2 and Fig. 5, the final closed-loop transfer function of the WPT system including a PI controller can be expressed as:

$$\Phi(s)=\frac{G_c(s)G(s)}{G_c(s)G(s)+1}=\frac{\omega_n^2}{z}\frac{(s+z)}{s^2+2\xi\omega_n+\omega_n^2}, \tag{25}$$

where the closed-loop zero $z=K_i/K_p$. In addition, ω_n and ξ are the natural frequency and damping ratio of the close loop poles. It can be seen that the proportion and integration elements of the controller are equivalent to adding a closed-loop zero and a new dominant pole to the low-order model (23). Therefore, the parameters of the controller can be calculated by arranging the time constant of the new closed-loop dominant pole with respect to the expected control performance.

By substituting (23) and (24) into (25), the characteristic equation of the final closed-loop transfer function can be expressed as:

$$\begin{aligned}&s^2+2\xi\omega_n+\omega_n^2=\left(s+\frac{1}{T_1}\right)\left(s+\frac{1}{T_2}\right)\\&=s^2+\left(3.1e4K_p+8.8e3\right)s+3.1e4K_i=0\end{aligned}, \tag{26}$$

TABLE II
REQUIREMENTS AND PARAMETERS OF PI CONTROLLERS

Controller	Desired Settling Time and Overshoot	K_p	K_i
(i)	50 ms and 0%	0.02	$K_{i(i)}$=22.7
(ii)	80 and 0%	0.02	$K_{i(ii)}$=14.1
(iii)	100 and 0%	0.02	$K_{i(iii)}$=11.4

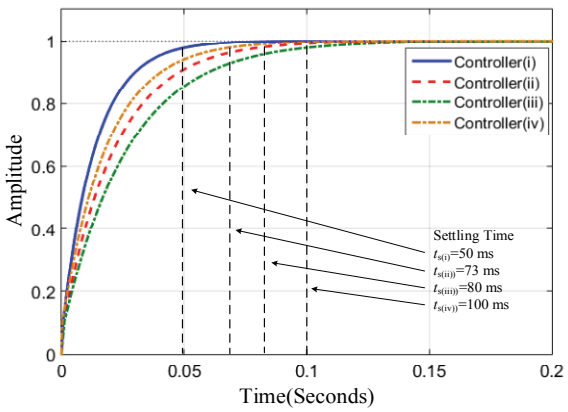

Fig. 6. Unit step response of a closed-loop system with the designed controllers (i)-(iii) and empirical equations based controller (iv).

where $T_1 \leq T_2$ is the time constant of the close loop poles.

In this paper, to validate the proposed controller design method, three different sets of control performance requirements are listed in Table II, where the error band Δ is selected to be 2%. Since an oscillation of the circuit exacerbates the EMI of the system, the overshoot of each controller is set to zero. According to the characteristics of the over-damped second-order linear system, the time constant of the dominant pole can be calculated by:

$$T_1 = 4 / t_s . \tag{27}$$

Thus, the relationship between K_p and K_i can be obtained by:

$$K_i = \frac{\left(3.1e4K_p + 8.8e3\right)/T_1 - \left(1/T_1\right)^2}{3.1e4} . \tag{28}$$

A proportional gain that is much smaller than unity is selected to be K_p=0.02 in this paper. According to (28), the integral coefficient K_i of each controller can be calculated as shown in Table II. In addition, in order to compare this with an existing method, an additional PI controller (iv) is designed based on the empirical method [16], [17]. According to the empirical equations of the Ziegler–Nichols method, the critical proportional coefficient K_{pcrit} and oscillation period T_{crit} of the model (22) can be obtained as 0.06 and 2.01×10^{-3}, respectively. This results in a proportional gain of $K_{p(iv)}$= 0.027 and an integral gain of $K_{i(iv)}$ = 16.2.

Fig. 6 shows the unit step response of a closed-loop system with the designed controllers (i)-(iii) and the empirical controller (iv). One obtains from the response curves that the unity feedback system responds to a step change with settling times $t_{s(i)}$=0.05 s, $t_{s(ii)}$=0.08 s, $t_{s(iii)}$=0.1 s, and no overshoot is observed, which satisfies expectations. In addition, the settling time of controller (iv) is about 0.073 s. This proves that the empirical controller can only achieve a stable and controllable system. Meanwhile, the proposed method can allocate the dominant poles and design the parameters according to preset performance requirements.

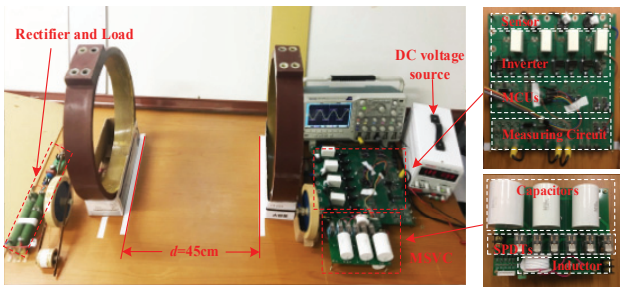

Fig. 7. Prototype of the proposed WPT system with a ZVS controller.

V. EXPERIMENTAL RESULTS

To validate the proposed controller design method, an experimental setup based on the topology circuit in Fig. 1 is built and tested. The prototype, shown in Fig. 7, consists of a DC voltage source, an MSVC, a full-bridge inverter, MCUs, an S-S resonant network, a full-bridge rectifier and several switchable loads. The main parameters of the components are shown in Table I, where the values of the mutual inductance and the ESR of the resonance network are measured using an LCR meter (Agilent 4263B) when the power transfer distance is 45 cm. Four IPW65R041CFD MOSFETs are used for the full-bridge inverter, and the PI controller is implemented with two MCUs. The MCUs are an FPGA (XC6SLX9-3TQG144I) and an ARM (STM32F407VGT). The diameters of the two coaxial epoxy resin coils are 38 cm, and the diameter of the Litz-wire consisting of 2000 isolated strands is 6 mm. For the battery load, resistors in parallel with a switch are used to simulate changes in the resistance during the charging process. By controlling the opening or closing of the switch, the load resistance can be conveniently changed.

A. Experiment of a Five-Stage MSVC

In order to implement the IMC method, a five-stage MSVC is developed in the experiment. This is done considering the regulation range and precision of the equivalent capacitance. Then, the relationship between the equivalent capacitance C_{1e} and the control quantity d, and the relationship between the ZVS angle and the equivalent capacitance C_{1e} are simulated and tested. The capacitors and SPDT relays are EACO STD 2000V and OMRON G2R-1-H5VDC. In the capacitor array of the five-stage MSVC, the maximum capacitance C_a is 2 μF. According to equation (14), the inductance L_a is calculated to

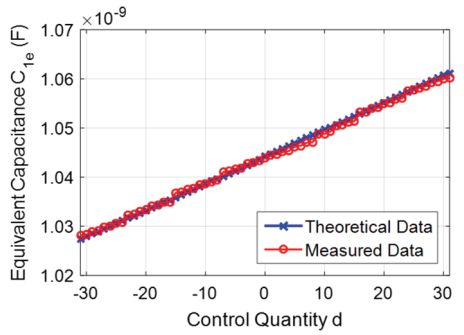

(a)

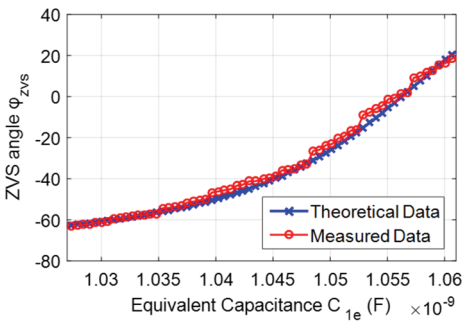

(b)

Fig. 8. Theoretical and measured data of the equivalent capacitance and the phase difference. (a) Equivalent capacitance C_{1e} vs. decimal controlling quantity d. (b) Phase difference $\Delta\varphi$ vs. equivalent capacitance C_{1e}.

be 2.18 μH.

Fig. 8(a) shows the relationship between the control quantity d and the equivalent capacitance C_{1e} from (15) and (16) by using the parameters of the components shown in Table I.

It can be seen that the theoretical curve of C_{1e} monotonically increases from 1029 pF to 1063 pF while d increases from -31 to 31. The measured data in Fig. 8(a) is consistent with the theoretical curve. According to (3) and (4), the relationship between C_{1e} and the ZVS angle φ_{zvs} is depicted in Fig. 8(b). Similarly, when C_{1e} monotonically increases 1029 pF to 1063 pF, the predicted and measured range of φ_{zvs} is in good agreement from -62.7° to 20.4°.

B. Performance of the Designed ZVS Controllers

In order to simulate the change of the ESR of the lead battery during the whole charging process [1]-[4] and to verify the control performance of the ZVS controller, three cases of step-changing loads are set up in this section. These cases are (I) from 5 Ω to 10 Ω, (II) from 10 Ω to 15 Ω and (III) from 15 Ω to 20 Ω. The data of the ZVS angle is calculated and saved by the MCUs and an RS232 communication circuit at a period of 10 ms.

The response of the ZVS angle φ_{zvs} to load cases (I), (II) and (III) with and without a controller (i)-(iv) is depicted in Fig. 9(a), (b) and (c). Without controllers, the ZVS angle deviates from the preset reference angle when the load resistance changes. Although the ZVS angle in each set of

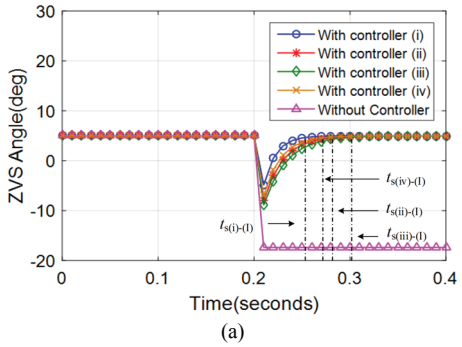

(a)

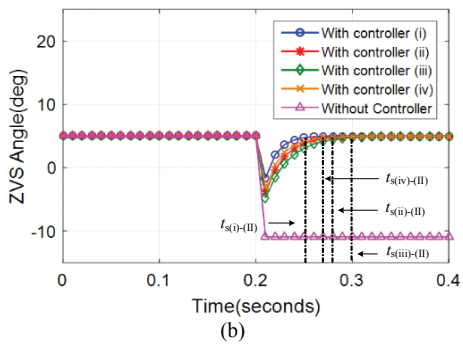

(b)

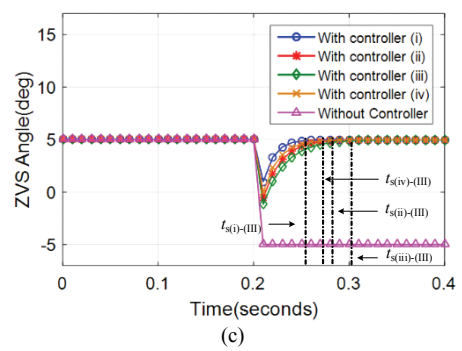

(c)

Fig. 9. Dynamic curves of the ZVS angle response to step changing loads. (a) Load case (I). (b) Load case (II). (c) Load case (III).

experiments drops rapidly, it gradually returns to the reference of 5° with the help of controllers, and no overshoot is observed. This proves that ZVS operation can be achieved by the designed controllers.

Table III records the settling time and overshoot of each set of experiments when an error band of 2% is selected. It can be seen from Table III that the control performances of the controllers (i), (ii), (iii) and (iv) are in good agreement with the simulation results in Fig. 6. When compared to the empirical controller (iv), Table III indicates that the proposed controller design method can allocate the dominant poles and design the parameters according to preset performance requirements.

Notably, when compared with controller (ii), the settling times of controllers (i) and (iii) are longer than the requirements. The same trend can also be found in controller (iv). This is because the parameters of controllers (i)-(iii) and the critical proportional coefficient K_{pcrit} of controller (iv) are all designed at a static operating point, where the load is 10 Ω. When the load changes, the operating point of the system

TABLE III
CONTROL PERFORMANCE OF CONTROLLERS (I), (II) AND (III) IN DIFFERENT LOAD CASES

Settling Time	Load (I)	Load (II)	Load (III)
$t_{s(i)}$	51 ms	50 ms	52 ms
$t_{s(ii)}$	82 ms	80 ms	84 ms
$t_{s(iii)}$	102 ms	100 ms	105 ms
$t_{s(iv)}$	73 ms	71 ms	72 ms

deviates from the point where the controller is designed. Therefore, the control performance of the controller is weakened. For this reason, research will be conducted in the future on system precise linearization and an advanced nonlinear controller design.

C. *Efficiency of the System*

According to [1], [3], [31], [33], transmission efficiency can be calculated by the overall power loss of both sides and the output power obtained from the load as:

$$\eta = \frac{P_{\text{load}}}{P_{\text{load}} + P_{\text{loss}}}, \tag{29}$$

where P_{load} is the power obtained from the load that can be achieved by measuring the voltage across the load. $P_{\text{loss}} = P_{\text{Ploss}} + P_{\text{Sloss}}$ is the overall power loss of both sides.

The power loss of the primary side P_{Ploss} consists of the primary side conduction loss P_{Pconduct} and the full-bridge inverter switching loss P_{inv}, which can be expressed as:

$$\begin{aligned} P_{\text{Pconduct}} &= \frac{I_1^2 R_1}{2} \\ P_{\text{inv}} &= 4\left(P_{\text{pton}} + P_{\text{ptoff}}\right) \\ &= \frac{40}{3} f_s C_{\text{ds}} \sqrt{V_I^3} + 4 f_s V_1 I_1 \left(\frac{t_r}{3} + \frac{t_f}{2}\right) \end{aligned} . \tag{30}$$

The symbols P_{pton} and P_{ptoff} represent the inverter turn-on and turn-off switching losses per transistor, which have been described in [31]. t_r and t_f represent the rising and falling times of the MOSFET, respectively. The MOSFET's drain-source capacitance C_{ds} is the capacitance of the body-drain PN step junction diode.

For the secondary side [33], the overall power loss P_{Sloss} consists of the secondary side conduction loss P_{Sconduct} and the rectifier power loss P_{rec}, which can be expressed as:

$$\begin{aligned} P_{\text{Sconduct}} &= \frac{I_2^2 R_2}{2} \\ P_{\text{rec}} &= 2\sqrt{2} V_{\text{Cf}} I_2 + \frac{r_{\text{Cf}} I_2^2}{2}\left(\frac{\pi^2}{8} - 1\right) \end{aligned} . \tag{31}$$

The symbol r_{Cf} represents the ESR of the rectifier diodes and filter capacitor. V_{Cf} stands for the forward voltage of the rectifier diodes. I_1 and I_2 are the magnitudes of i_1 and i_2, which can be acquired by a hall sensor and a measuring circuit. According to the parameters of the system components in Table I, it is possible to obtain the transmission efficiency with and without the designed controller.

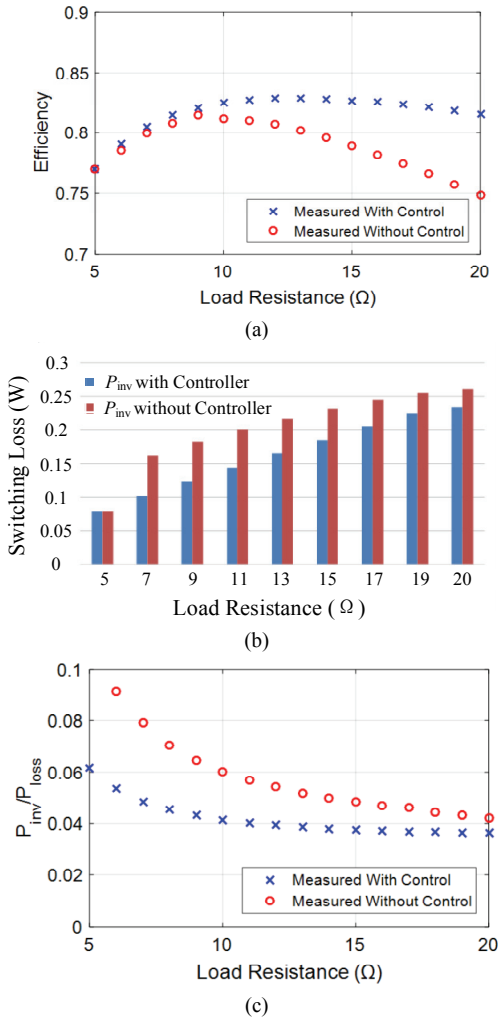

Fig. 10. Curves of transmission efficiency and inverter switching loss. (a) Transmission efficiency versus a changing load with and without control. (b) Inverter switching power loss with and without control. (c) Ratio of the inverter switching loss P_{inv} to the overall loss of both sides P_{loss} with and without control.

Taking controller (ii) as an example, Fig. 10(a) presents the transmission efficiency versus a changing load from 5 Ω to 20 Ω with and without control. It can be seen that the controller enables the system to achieve a higher transmission efficiency. Benefiting from the controller, the maximum system efficiency can reach 83%. This is because the impedance matching allows the system to operate in an optimized state. The inverter switching power loss with and without control versus the load resistance is calculated and plotted in Fig. 10(b). When R_b increases, it can be seen that P_{inv} with control is lower than that without control. This is because the ZVS angle can be maintained at the preset reference angle. Thus, P_{pton} is zero and only P_{ptoff} is taken into consideration. To clarify the contribution of P_{inv} to the system transmission efficiency, a ratio curve of P_{inv} to P_{loss} with and without control is plotted in Fig. 10(c). It can be seen that the designed controller results in a lower ratio of P_{inv} to P_{loss}.

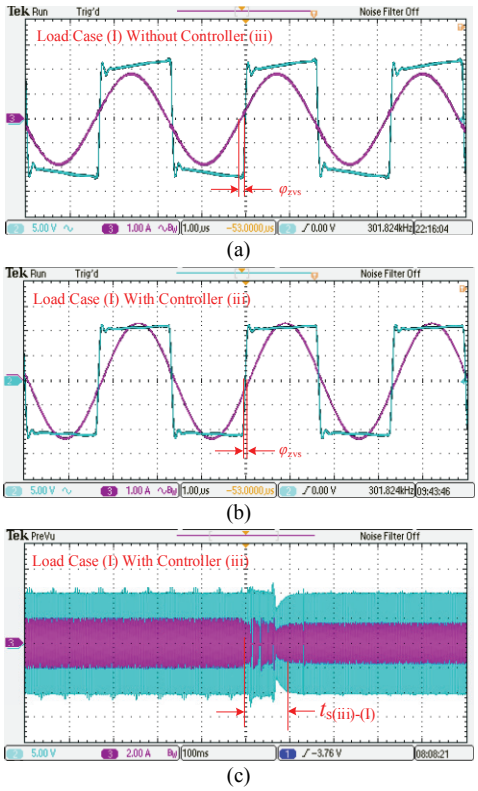

(a) (b) (c)

Fig. 11. Dynamic and steady-state waveforms of i_1 and v_{ab} under load case (I). (a) φ_{zvs} without controller (iii); (b) φ_{zvs} with controller (iii). (c) Dynamic waveforms of i_1 and v_{ab} with controller (iii).

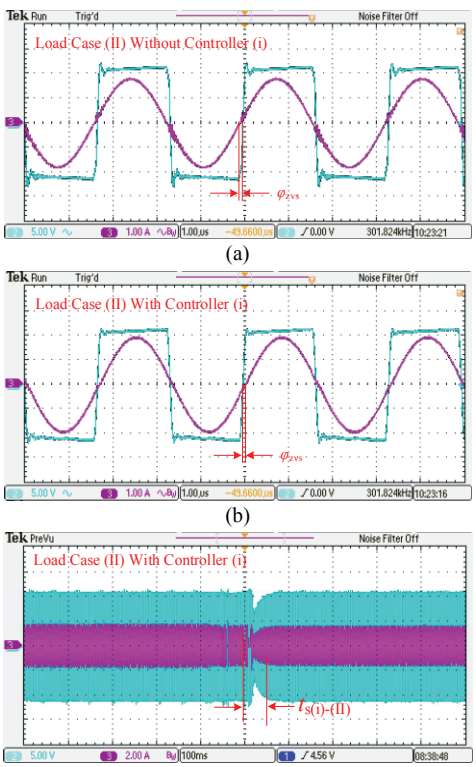

(a) (b) (c)

Fig. 12. Dynamic and steady-state waveforms of i_1 and v_{ab} under load case (II). (a) φ_{zvs} without controller (i). (b) φ_{zvs} with controller (i). (c) Dynamic waveforms of i_1 and v_{ab} with controller (i).

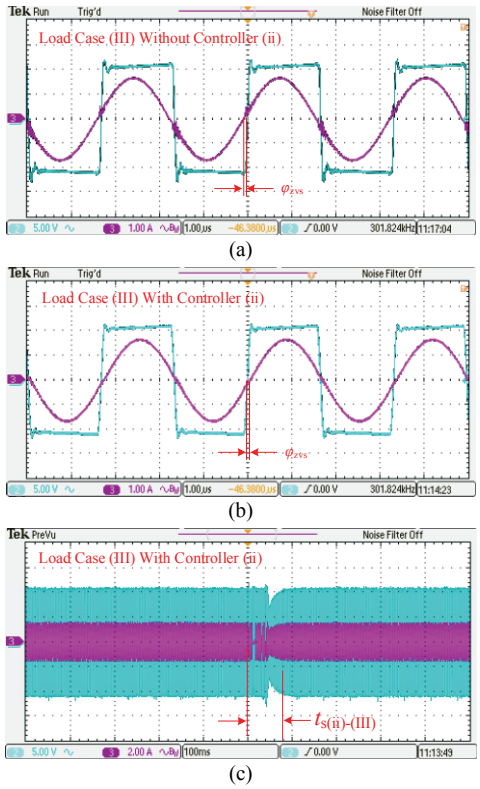

(a) (b) (c)

Fig. 13. Dynamic and steady-state waveforms of i_1 and v_{ab} under load case (III). (a) φ_{zvs} without controller (ii). (b) φ_{zvs} with controller (ii). (c) Dynamic waveforms of i_1 and v_{ab} with controller (ii).

D. Output Waveform Analysis

Steady-state and dynamic waveforms of i_1 and v_{ab} in different load cases with/without the designed controllers are captured by an oscilloscope (Tektronix DPO 2004B) and shown in Fig. 11 through Fig. 13. In detail, Fig. 11(a) and (b) depict steady-state waveforms of i_1 and v_{ab} in load case (I) with and without the control. It can be seen from Fig. 11(a) that the ZVS operation is doomed to fail when there is no control. Conversely, the ZVS angle φ_{zvs} in Fig. 11(b) can be maintained at the preset reference angle by the designed controller. Fig. 11(c) shows dynamic waveforms of i_1 and v_{ab} during an adjustment of the MSVC with controller (iii). It can be seen that the settling time of the adjustment is about 100 ms, which is in good agreement with the performance requirements in Table II.

Fig. 12 and Fig. 13 exhibit waveforms captured in load cases (II) and (III). The same trend can be observed in Fig. 12(a) and Fig. 13(a) when the load resistance changes. The phase angle of the current lags behind the voltage when there is no controller. In addition, with controllers (i) and (ii), the ZVS angles in Fig. 12(b) and Fig. 13(b) can track the reference values and stay constant in spite of changes in the load. Meanwhile, the settling times of the adjustment in Fig. 12(c) and Fig. 13(c) are about 50 ms and 80 ms, respectively. These results are also consistent with the performance requirements in Table III.

VI. CONCLUSIONS

In this paper, a model-based ZVS controller design method was proposed and implemented for WPT systems. Based on the zero-pole distribution of the model, the dynamic performance of the ZVS angle was analyzed. In order to facilitate the controller design, a low-order equivalent transfer function model that consists of dominant poles was obtained. Unlike existing methods, the parameters of the ZVS controllers in this paper were designed by calculating the time constant of the closed loop dominant poles according to requirements. Therefore, the ZVS controllers were especially useful when the system required tight designing in terms of its preset settling time and overshoot. In the experiment, a five-stage MSVC was constructed to act as an actuator for the controllers. The recorded response curves and steady-state waveforms demonstrated that the ZVS angle can be maintained at the reference angle with an expected control performance when the load step changes. Although IMC was the main concern in this paper, the proposed modeling and the designing method of the ZVS controller can be applied to FC or a hybrid control method. In addition, a precise linearization and an advanced nonlinear controller design method that are independent of the operating point will be studied in the future to overcome fluctuations in the controller performance.

APPENDIX

$$K_1 = \sqrt{L_1 / 2} / \left(L_1 L_2 - M^2 \right)$$
$$K_2 = \sqrt{L_2 / 2} / \left(L_1 L_2 - M^2 \right)$$

$$K_3 = R_1 x_1 / \sqrt{2L_1}$$
$$K_4 = x_3 / \sqrt{2C_2}$$
$$K_5 = \left(R_2 + R_{cd} \right) x_3 / \sqrt{2L_2}$$
$$K_6 = 2V_I / \pi$$
$$K_7 = -1 / \left(2 \left(\sqrt{C_{1e}} \right)^3 \right)$$
$$K_8 = \sin\left(x_2 - x_4 \right)$$
$$K_9 = \cos\left(x_2 - x_4 \right)$$

ACKNOWLEDGMENT

This work is supported by National Natural Science Foundation of China under Grant 51677139 and Grant 61873195.

REFERENCES

[1] Q. Deng, J. Liu, D. Czarkowski, M. Bojarski, E. Asa, and F. de Leon, "Design of a wireless charging system with a phase-controlled inverter under varying parameters," *IET Power Electron*., Vol. 9, No. 13, pp. 2461-2470, Oct. 2016.

[2] F. Musavi and W. Eberle, "Overview of wireless power transfer technologies for electric vehicle battery charging," *IET Power Electron.*, Vol. 7, No. 1, pp. 60-66, Jan. 2014.

[3] Y. Jiang, L. Wang, Y. Wang, J. Liu, X. Li, and G. Ning, "Analysis, design and implementation of accurate ZVS angle control for EV's battery charging in wireless high power transfer," *IEEE Trans. Ind. Electron.*, Vol. 66, No. 5, pp. 4075-4085, May 2019.

[4] T. Chan and C. Chen, "A primary side control method for wireless energy transmission system," *IEEE Trans. Circuits Syst. I: Reg. Papers*, Vol. 59, No. 8, pp. 1805-1814, Aug. 2012.

[5] Q. Chen, S. C. Wong, C. K. Tse, and X. Ruan, "Analysis, design, and control of a transcutaneous power regulator for artificial hearts," *IEEE Trans. Biomed. Circuits Syst.*, Vol. 3, No. 1, pp. 23-31, Jan. 2009.

[6] J. Park, D. Kim, K. Hwang, H. H. Park, S. I. Kwak, J. H. Kwon, and S. Ahn, "A resonant reactive shielding for planar wireless power transfer system in smartphone application," *IEEE Trans. Electromag. Compat.*, Vol. 59, No. 2, pp. 695-703, Jan. 2017.

[7] T. Mishima and E. Morita, "High-frequency bridgeless rectifier based ZVS multiresonant converter for inductive power transfer featuring high-voltage GaN-HFET," *IEEE Trans. Ind. Electron.*, Vol. 64, No. 11, pp. 9155-9164, Nov. 2017.

[8] S. Iguchi, P. Yeon, H. Fuketa, K. Ishida, T. Sakurai, and M. Takamiya, "Wireless power transfer with zero-phase-difference capacitance control," *IEEE Trans. Circuits Syst. I, Regul. Papers*, Vol. 62, No. 4, pp. 938-947, Apr. 2015.

[9] P. Si, A. P. Hu, S. Malpas, and D. Budgett, "A frequency control method for regulating wireless power to implantable devices," *IEEE Trans. Biomed. Circuits Syst*., Vol. 2, No. 1, pp. 22-29, Apr. 2008.

[10] J. Tian and A. P. Hu, "A DC-voltage-controlled variable capacitor for stabilizing the ZVS frequency of a resonant converter for wireless power transfer," *IEEE Trans. Power Electron*., Vol. 32, No. 3, pp. 2312-2318, Mar. 2017.

[11] Z. Miao, D. Liu, and C. Gong, "An adaptive impedance matching network with closed loop control algorithm for inductive wireless power transfer," *Sensors*, Vol. 17, No. 8, pp. 1759, Aug. 2017.

[12] T. C. Beh, M. Kato, T. Imura, S. Oh, and Y. Hori, "Automated impedance matching system for robust wireless power transfer via magnetic resonance coupling," *IEEE Trans. Ind. Electron*., Vol. 60, No. 9, pp. 3689-3698, Sep. 2013.

[13] Y. Lim, H. Tang, S. Lim, and J. Park, "An adaptive impedance-matching network based on a novel capacitor matrix for wireless power transfer," *IEEE Trans. Power Electron*., Vol. 29, No. 8, pp. 4403-4413, Aug. 2014.

[14] J. Ren, P. Hu, D. Yang, and D. Liu, "Tuning of mid-range wireless power transfer system based on delay-iteration method," *IET Power Electron*., Vol. 9, No. 8, pp. 1563-1570, Jun. 2016.

[15] J. U. W. Hsu, A. P. Hu, and A. Swain, "Fuzzy logic-based directional full-range tuning control of wireless power pickups," *IET Power Electron*., Vol. 5, No. 6, pp. 773-781, Jul. 2012.

[16] J. Shin, S. Shin, Y. Kim, S. Ahn, S. Lee, G. Jung, S. J. Jeon, and D. H. Cho, "Design and implementation of shaped magnetic-resonance-based wireless power transfer system for roadway-powered moving electric vehicle," *IEEE Trans. Ind. Electron*., Vol. 61, No. 3, pp. 1179-1192, Mar. 2014.

[17] B. Wang, A. P. Hu, and D. Budgett, "Maintaining middle zero voltage switching operation of parallel-parallel tuned wireless power transfer system under bifurcation," *IET Power Electron*., Vol. 7, No. 7, pp. 78-84, Jan. 2014.
[18] P. Tan, H. He, and X. Gao, "A frequency-tracking method based on a SOGI-PLL for wireless power transfer systems to assure operation in the resonant state," *J. Power Electron.*, Vol. 16, No. 3, pp. 1056-1066, May 2016.
[19] S. Lee, B. Choi, and C. T. Rim, "Dynamics characterization of the inductive power transfer system for online electric vehicles by Laplace phasor transform," *IEEE Trans. Power Electron*., Vol. 28, No. 12, pp. 5902-5909, Dec. 2013.
[20] Z. Huang, S. C. Wong, and C. K. Tse, "Control design for optimizing efficiency in inductive power transfer systems," *IEEE Trans. Power Electron*., Vol. 33, No. 5, pp. 4523-4534, May. 2018
[21] H. Hao, G. A. Covic, and J. T. Boys, "An approximate dynamic model of LCL-T-based inductive power transfer power supplies," *IEEE Trans. Power Electron*., Vol. 29, No. 10, pp. 5554-5567, Oct. 2014.
[22] R. Tavakoli and Z. Pantic, "Analysis, design and demonstration of a 25-kW dynamic wireless charging system for roadway electric vehicles," *IEEE J. Emerg. Sel. Topics Power Electron*., Vol. 6, No. 3, pp.1378-1393, Sep. 2018.
[23] Z. U. Zahid, Z. M. Dalala, C. Zheng, R. Chen, W. E. Faraci, J. S. J. Lai, G. Lisi, and D. Anderson, "Modeling and control of series-series compensated inductive power transfer system," *IEEE J. Emerg. Sel. Topic Circuits Syst*., Vol. 3, No. 1, pp. 111-123, Mar. 2015.
[24] A. K. Swain, M. J. Neath, U. K. Madawala, and D. J. Thrimawithana, "A dynamic multivariable state-space model for bidirectional inductive power transfer systems," *IEEE Trans. Power Electron*., Vol. 27, No. 11, pp. 4772-4780, Nov. 2012.
[25] A. P. Hu, "Modeling a contactless power supply using GSSA method," *Proc. ICIT*, pp. 500-505, Feb. 2009.
[26] M. M. Rana, W. Xiang, E. Wang, and B. J. Choi, "The internet of things infrastructure for wireless power transfer systems," *IEEE Access*, Vol. 6, pp. 19295-19303, Jan. 2018.
[27] Y. Li, J. Hu, F. Chen, Z. Li, Z. He, and R. Mai, "Dual-phase-shift control scheme with current-stress and efficiency optimization for wireless power transfer systems," *IEEE Trans. Circuits Syst. I: Reg. Papers*, Vol. 65, No. 9, pp. 3110-3121, Sep. 2018.
[28] A. Kurs, A. Karalis, R. Moffatt, J. D. Joannopoulos, P. Fisher, and M. Soljačić, "Wireless power transfer via strongly coupled magnetic resonances," *Science*, Vol. 317, No. 5834, pp. 83-86, Jun. 2007.
[29] H. Li, K. Wang, L. Huang, W. Chen, and X. Yang, "Dynamic modeling based on coupled modes for wireless power transfer systems," *IEEE Trans. Power Electron*., Vol. 30, No. 11, pp. 6245-6253, Nov. 2015.
[30] H. Li, J. Li, L. Huang, K. Wang, and X. Yang, "A novel dynamic modeling method for wireless power transfer systems," *Proc. APEC*, pp. 2740-2743, May. 2015.
[31] M. K. Kazimierczuk and D. Czarkowski, *Resonant Power Converters*, Chap. 6, John Wiley & Sons, 2011,
[32] Q. Deng, J. Liu, D. Czarkowski, M. K. Kazimierczuk, M. Bojarski, H. Zhou, and W. Hu, "Frequency-dependent resistance of litz-wire square solenoid coils and quality factor optimization for wireless power transfer," *IEEE Trans. Ind. Electron*., Vol. 63, No. 5, pp. 2825-2837, May. 2016.
[33] Q. Deng, J. Liu, D. Czarkowski, W. Hu, and H. Zhou, "An inductive power transfer system supplied by a multiphase parallel inverter," *IEEE Trans. Ind. Electron*., Vol. 64, No. 9, pp. 7039-7048, Sep. 2017.

Cheng Chen was born in China, in 1989. He received his B.S. degree in Mechanical Engineering from Wuhan Institute of Bioengineering, Wuhan, China, in 2012; and his M.S. degree in Control Engineering from Wuhan University, Wuhan, China, in 2015, where he is presently working towards his Ph.D. degree in the School of Electrical Engineering and Automation. His current research interests include system modeling, nonlinear control and wireless power transfer.

Hong Zhou was born in China, in 1962. He received his B.S. degree from the Central South University of Technology (now Central South University), Changsha, China, in 1982; his M.S. degree from Chongqing University, Chongqing, China, in 1988; and his Ph.D. degree from Wuhan University, Wuhan, China, in 2006. He was an Assistant Engineer at the Changshou Power Plant, Chongqing, China, from 1982 to 1985. He has been at the Wuhan University of Hydraulic and Electrical Engineering (now a part of Wuhan University), Wuhan, China, since 1992. He was the Head of the Department of Automation at Wuhan University from 2002 to 2006, and has been a Professor in that department since 2000. His current research interests include wireless power transfer, smartgrids and networked control systems.

Qijun Deng was born in China, in 1975. He received his B.S. and M.S. degrees in Mechanical Engineering, and his Ph.D. degree in Computer Application Technology from Wuhan University, Wuhan, China, in 1999, 2002 and 2005, respectively. In June 2005, he joined the Department of Automation (which has since merged into the School of Electrical Engineering and Automation), Wuhan University, where he is presently working as a Professor. From 2013 to 2014, he was a Visiting Scholar at New York University Tandon School of Engineering, Brooklyn, NY, USA. His current research interests include wireless power transfer, distribution automation and electrical power informatics.

Wenshan Hu was born in China, in 1980. He received his B.S. and M.S. degrees in Control Theory and Applications from Wuhan University, Wuhan, China, in 2002 and 2004, respectively. He received his Ph.D. degree in Control Engineering from the University of Glamorgan, Pontypridd, WLS, UK, in 2008. He is presently working as a Professor in the Department of Automation, School of Electrical Engineering and Automation, Wuhan University. His current research interests include wireless power transfer and network-based control laboratories.

Yanjuan Yu was born in China, in 1991. She received her B.S. degree in Control Theory and Applications from Wuhan University, Wuhan, China, in 2013, where she is presently working towards her Ph.D. degree in the School of Electrical Engineering and Automation. Her current research interests include wireless power transfer, mathematical optimization, renewable energy accommodation and integrated energy systems.

Xiaoqing Lu received her Ph.D. degree in Applied Mathematics from Wuhan University, Wuhan, China, in 2012. She is presently working as a Professor in the Department of Automation, School of Electrical Engineering and Automation, Wuhan University. Her current research interests include cyber-physical systems, microgrids, intelligent systems and applications, nonlinear dynamical systems and multi-agent systems.

Jingang Lai received his Ph.D. degree in Control Science and Engineering from Wuhan University, Wuhan, China, in 2016. He was a joint Ph.D. student in the School of Electrical and Computer Engineering, RMIT University, Melbourne, VIC, Australia, in 2015. He is presently working as a Research Fellow in the E.ON Energy Research Center, RWTH Aachen University, Aachen, Germany. His current research interests include distributed intelligence for smartgrids and networked control systems.